Tuning vortex confinement by magnetic domains in a superconductor/ferromagnet bilayer

Marta Z. Cieplak,[1,2] Z. Adamus,[1,3] M. Końc zykowski,[3] L. Y. Zhu,[2,*] X. M. Cheng,[2,4] and C. L. Chien[2]

[1]*Institute of Physics, Polish Academy of Sciences, 02 668 Warsaw, Poland*
[2]*Department of Physics and Astronomy, The Johns Hopkins University, Baltimore, Maryland 21218, USA*
[3]*Laboratoire des Solides Irradies, École Polytechnique, 91128 Palaiseau, France*
[4]*Department of Physics, Bryn Mawr College, Bryn Mawr, Pennsylvania 19010-2899, USA*

We use a line of miniature Hall sensors to study the effect of magnetic-domain-induced vortex confinement on the flux dynamics in a superconductor/ferromagnet bilayer. A single tunable bilayer is built of a ferromagnetic Co/Pt multilayer with perpendicular magnetic anisotropy and a superconducting Nb layer, with the insulating layer in-between to avoid the proximity effect. The magnetic-domain patterns of various geometries are reversibly predefined in the Co/Pt multilayer using the appropriate magnetization procedure. The magnetic-domain geometry strongly affects vortex dynamics, leading to geometry-dependent trapping of vortices at the sample edge, nonuniform flux penetration, and strongly nonuniform critical current density. With the decreasing temperature, the magnetic pinning increases, but this increase is substantially weaker than that of the intrinsic pinning. The analysis of the initial flux penetration suggests that vortices may form various vortex structures, including disordered Abrikosov lattice or single and double vortex chains, in which minimal vortex-vortex distance is comparable to the magnetic penetration depth.

PACS number(s): 74.25.Ha, 74.25.Wx, 74.78.Fk

I. INTRODUCTION

The behavior of vortices in type-II superconductors depends on the interplay of the repulsive vortex-vortex (v-v) interactions and the interaction of vortices with the pinning potential. In the absence of pinning, the vortices arrange themselves into a triangular Abrikosov lattice.[1] The pinning may greatly alter this arrangement, leading to formation of disordered vortex matter[2,3] or rectangular or more complicated vortex lattices.[4–6] A different and more interesting case is the pinning potential which leads to the confinement of vortices to isolated islands, resembling the confinement observed in mesoscopic superconductors.[7,8] Examples of such confinement include the reports on thin Nb films with perforated or blind microholes[9] and, more recently, on single-crystal $NbSe_2$ with an array of Au islands on the top.[10]

A model confining potential may be realized in the planar superconductor/ferromagnet (S/F) bilayer (SFB), in which the magnetic domains in the F layer create pinning potential for vortices.[6,11–20] When the F layer exhibits perpendicular magnetic anisotropy (PMA) with a well-defined direction of the magnetic moment of the domain, the vortices are selectively attracted to the domains of one sign.[21–32] Recently, several experiments demonstrated formation of single or multiple vortex chains confined to domains of one sign in SFB's with stripe domain patterns, in which an equal amount of $+/-$ domains exist. These experiments include imaging with scanning tunneling microscopy[27] (STM) and low-temperature magnetic force microscopy[31] (MFM), as well as magnetotransport measurements.[28]

A related issue is the influence of vortex confinement on flux motion in the superconductor. In the bulk samples and on a macroscopic scale, the flux entry is usually smooth except for thermomagnetic instabilities which occur at low temperatures.[33,34] However, the imaging of flux on a local scale reveals much larger complexity. Flux inhomogeneities in the form of various edge barriers are common,[35] and

sometimes flux droplets or twisters are observed.[36–38] The formation of vortex chains has been reported in anisotropic layered superconductors and in artificial multilayers.[39–43] Inhomogeneous flux penetration leading to commensurability or channeling effects has been well documented for ordered or quasiordered arrays of pinning centers,[5,6] while in the case of SFBs with stripe domain patterns, anisotropic flux entry has been observed.[24,44] Recently, irregular flux penetration in the form of a terraced critical state has been observed by scanning Hall microscopy in thin Pb film with an array of antidots,[45] in agreement with theoretical predictions.[46,47]

In this work, we show interesting examples of vortex confinement occurring in the SFBs in which the amount of $+/-$ domains has been purposely made to be greatly unequal, so that the domains of one sign are immersed in the background of the opposite sign. We use a planar SFB, in which the S layer is Nb and the F layer is Co/Pt multilayer with PMA. In this SFB, the various domain patterns, with different domain width w, domain length L, and the amount of $+/-$ domains, are reversibly predefined and erased through the partial magnetic reversal process as previously described.[22] This allows studies of the influence of the domain geometry on the vortex behavior in a single tunable sample. We use a line of miniature Hall sensors placed across the S layer to probe locally the dependence of the magnetic induction B and the critical current density J_c on the distance x from the sample edge, as the external magnetic field H is cycled. We show that for some domain patterns, $B(x)$ forms an irregular profile across the sample width, and the critical current density is strongly nonuniform, suggesting that some commensurability effects occur on a local scale. When the flux first enters the S layer it becomes trapped on the domains in the vicinity of the sample edge. The analysis of this effect shows that the vortices most likely arrange themselves into distinct patterns, including single or double vortex chains or the Abrikosov lattice, depending on the domain dimensions and the amount of $+/-$ domains.

II. EXPERIMENTAL DETAILS

The SFB was grown at room temperature by sputtering on Si substrate, with the layer sequence Si(10)/Pt(10)/[Co(0.4)/Pt(1)]$_8$/Si(10)/Nb(78), where the thickness is denoted in nanometers. The sample structure is shown schematically in Fig. 1(a). The surface roughness of the structure has been measured to be in the range 0.1 to 0.3 nm. The Si layer between Co/Pt and Nb serves as a buffer to eliminate the proximity effect. Prior to this experiment, we have checked that the superconducting transition temperature (T_c) of the Nb film is not influenced by a thin Si overlayer, which proves that the proximity effect between Nb and Si is negligible. We have also verified that the SFB studied here exhibits T_c higher by about 0.8 K in comparison with identical SFB but without the Si buffer, indicating that the Si buffer cuts off the proximity effect between F and S layers.

The magnetization of the sample has been measured using a commercial SQUID magnetometer. Shown in Fig. 1(b) is a square hysteresis loop of the Co/Pt multilayer measured with the magnetic field perpendicular to the sample surface, at temperature $T = 300$ K. The coercive field is $H_C \approx 300$ Oe at 300 K, and increasing to $H_C \approx 750$ Oe when the sample is cooled to 10 K. The vertical scale shows rescaled magnetization describing the partial reversal of the magnetic moment, $s = (M/M_s + 1)/2$, with M and M_s as the magnetization and the magnetization at saturation, respectively. For a saturated F layer, s is equal to 0 or 1. The labels **a** to **h** in Fig. 1(b) indicate several states of the F layer with intermediate magnetization, when $+$ and $-$ domains coexist. These states are obtained by the partial reversal process, as already described by us and others.[21,22] For example, to set the state labeled by **a**, the sample is magnetized first to saturation ($s = 1$) by applying large positive field ($H = +2$ T). Then, the magnetic

field is lowered to zero, reversed, and increased towards the vicinity of $-H_C$, when s starts to drop. After reaching the value of s of about 0.91, the increase of the field is stopped, and subsequently the field is slowly decreased to zero. The magnetization is measured continuously to monitor the relaxation, which usually occurs. However, if the magnetic field is ramped slowly, the relaxation is small. After the magnetization is relaxed, the s value is calculated, and the magnetic-domain pattern created in the process is imaged by MFM. The domain pattern remains stable during imaging.

To characterize the superconducting properties of the Nb layer, magnetoresistance has been measured for the SFB magnetized to saturation ($s = 0$ or 1). The measurements, in the T range from 4 to 300 K, and in the perpendicular magnetic field ranging from 0 to 5 T, have been done using the same magnetometer, with the sample attached to a resistance measuring probe. From these measurements, we extract the $T_c = 8.73$ K, and, from the dependence of the upper critical field on temperature, the coherence length $\xi(0) = 13.2$ nm. We then estimate the Ginzburg-Landau parameter $\kappa \approx 4.6$. For this estimate, we use standard formulas for the dirty-limit superconductors[48] $\kappa = 0.715\lambda_L(0)/l$ and $\xi(0) = 0.855\sqrt{\xi_0 l}$. Here, $\xi_0 = 39.5$ nm and $\lambda_L(0) = 39$ nm are BCS coherence length and London penetration depth for bulk Nb, respectively,[49,50] and $l = 6.1$ nm is the mean-free path in the film, extracted from the second of the above formulas. Next, we proceed to estimate the T-dependent magnetic penetration depth $\lambda(T) \sim \kappa\xi(0)/\sqrt{1 - T/T_c}$ (Ref. 48) and the effective penetration depth $\Lambda = \lambda^2/t$, where t is the sample thickness. At temperatures used in our experiments, $T = 7.5$, 7, and 6.5 K, Λ is equal to about 331, 236, and 183 nm, respectively.

To study the flux entry in the superconducting state the sample is cut into a strip, 240 μm wide, and a line of nine miniature Hall sensors, 20 μm apart, is placed across the strip, as shown in Fig. 3(a). The $x = 0$ on the axis indicates the position of the first sensor, situated closest to the sample edge, but at a finite distance from it. The position $x = 120$ μm shows the sensor closest to the sample center. An additional sensor residing a few millimeters away from the line (shown away and to the left from the remaining sensors) measures the background signal. The Hall sensors, of the area $A_{sen} = 5 \times 5$ μm^2 each, are two-dimensional electron gas (2DEG) devices fabricated in a pseudomorphic AlGaAs/InGaAs/GaAs heterostructure. The sensitivity of all sensors is similar, limited by telegraphic noise to about 0.05 Gs on average. Occasionally, larger noise spikes may occur, triggered by the external noise influence on the metastable free carriers inside the sensor; these disturbances are rare and usually do not exceed ± 0.5 Gs. They are also easy to identify because they affect several adjacent sensors for a range of consecutive H values. A separate set of four contacts allows us to measure the s value using the anomalous Hall effect (AHE).
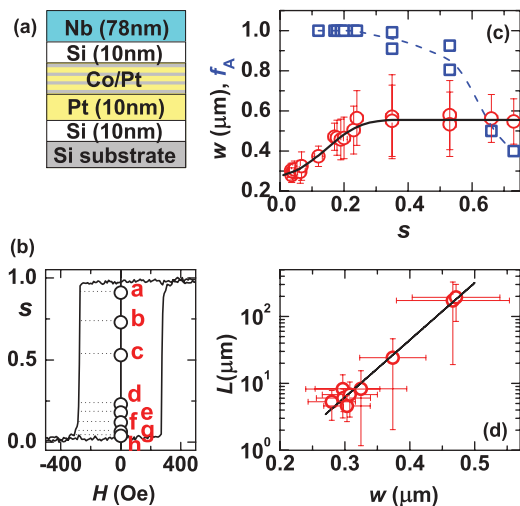

FIG. 1. (Color online) (a) Schematic drawing of the SFB. (b) Hysteresis loop of Co/Pt at 300 K. Vertical axis shows rescaled magnetization s, defined by $s = (M/M_s + 1)/2$, where M and M_s are the magnetization and the magnetization at saturation, respectively. The circles indicate s states imaged by MFM. (c) Domain width w (circles) and filling factor f_A (squares) versus s; the continuous line shows the fit to the data and the dashed line is a guide to the eye. (d) Domain length L versus w; line shows linear fit to the data.

III. RESULTS

A. Tuning the magnetic-domain patterns

The evolution of the domain pattern during the partial reversal process is shown in the MFM images [Figs. 2(a)–2(h)]. Prior to taking each image, the sample is magnetized, first to
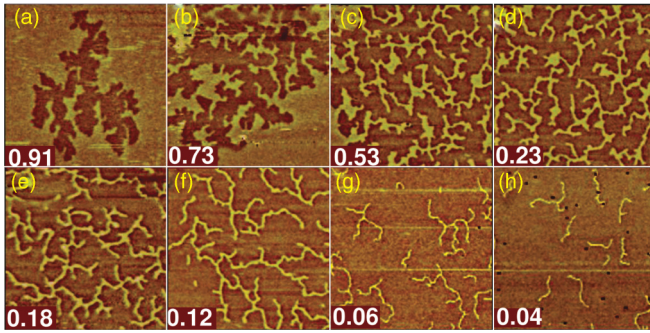
FIG. 2. (Color online) (a)–(h) MFM images (25×25 μm) of Co/Pt at 300 K for various s states indicated by the label.

saturation, then to a specific value of s indicated in Fig. 1(b) by open circles and labeled **a**–**h**. Image 2(a) (taken for $s = 0.91$, as indicated by the label) shows that the reversal starts from freshly inverted domain (dark) in the uninverted background (bright). On going from 2(a) to 2(d), the inverted areas expand until they spread to cover the whole image, with a maze of residual uninverted (RU) domains left behind. With further decrease of s, from Figs. 2(e) to 2(h), the dimensions of the RU domains decrease rapidly, until RU domains become narrow and well isolated.

When the inverted domains cover the whole image, as in the case of images 2(d)–2(h), we can estimate from the images the surface area of the RU domains (all estimates are based on the images of the size 50×50 μm). The ratio of the surface area of RU domains to the total image area agrees very well with the value of s measured by magnetometry.

For images 2(a)–2(c), we may estimate the fraction of the total image area, into which the inverted domains have spread f_A, which we call "filling factor"; in this case the surface area of the RU domains is given by $s f_A$. The factor f_A, shown by the open squares in Fig. 1(c), is seen to increase with decreasing s and saturate at 1 for $s \lesssim 0.25$. Note that several data points are plotted for each $s \gtrsim 0.37$. This is because different images taken on the same sample may lead to different f_A. For our estimate, we average over different f_A values obtained from several images for each s.

From MFM images, we have also estimated the average domain width w and domain length L for the RU domains, and the standard deviations Δw and ΔL. To get the estimate, many images are carefully analyzed. For each image, w has been measured in many places along each domain length, and based on this the average, w and Δw has been calculated. Figure 1(c) shows that w is about 0.55 μm and approximately constant at large s. When s decreases below 0.3, w starts to decrease, reaching a value of about 0.28 μm at $s = 0.04$. The estimate of L is not at all possible for $s \gtrsim 0.18$ ($w \gtrsim 0.47$ μm) because in these images a single domain with multiple branches reaches both sides of the image. With s decreasing below 0.18, the RU domains evolve, from dendrite-shaped domains with many branches to isolated short stripes at $s = 0.04$. The length of each branch has been measured and added to obtain the total L for each domain. Subsequently, the average L and ΔL have been extracted. They are plotted in Fig. 1(d) versus w. We see that L is at least an order of magnitude larger than w, and it decreases exponentially with the decrease of w.

Since the flux penetration study involves measurement across the thin sample strip, we have paid particular attention to the possible effect of the sample edge on the domain distribution or orientation. To evaluate this, we have compared the images taken in the sample center to those taken in the vicinity to the sample edge. We have found no difference between them.

Finally, we note that domains may shrink upon cooling. This shrinkage may be estimated based on the T dependence of M_s.[24] Using the measured $M_s(T)$ of our samples, we estimate that w shrinks at $T = 8$ K by less than 10%. In the following discussion of our experiment we therefore disregard this small change.

B. Flux penetration

The measurements of flux penetration proceed as follows. First, the RU domain pattern is predefined at $T = 10$ K by magnetizing the samples to a specific s value. After the field is removed, the sample is cooled just below T_c, and the measurements of $B(x)$ are performed simultaneously by all sensors while H is cycled, from 0 up to $+90$ Oe, from $+90$ Oe to -90 Oe, and from -90 Oe to 0. We have verified that this field, which is much smaller than H_C, has no effect on the s value.

To study the effect of RU domain polarity on the flux penetration, we distinguish between two processes of magnetic reversal: the s_+ (s_-) process is the one starting from $s = 1$ ($s = 0$), with the RU domains being positive (negative). This is depicted in the inset of Fig. 5, which shows a hysteresis loop measured by AHE at $T = 10$ K. Points specify some of the s_+ and s_- for which the flux entry have been studied (for clarity, not all the data are shown).

1. Inhomogeneous flux profile and critical current density

Figures 3(b)–3(g) show several flux profiles measured at $T = 7.5$ K across the sample [with the sample-sensors configuration depicted in Fig. 3(a)] during the initial increase of H from 0 to $+30$ Oe. The $x = 0$ on the horizontal axis, marked by a vertical (black) line, indicates the position of the first sensor, closest to the sample edge. The second vertical (red) line at $x = 120$ μm shows the position of the sensor closest to the sample center. The background data, measured by the sensor residing a few millimeters away from the sample, are shown on a vertical axis to the left of $x = 0$. These data give us a value of the external magnetic field H in the sample space.

The two topmost Figs. 3(b) and 3(c) depict the flux profiles for the F layer magnetized to saturation $s_+ = 0.99$ and $s_- = 0.01$. Most of the profiles shown in these figures are smooth, but occasionally jumps appear, which do not exceed ± 1 Gs. These jumps are randomly distributed so they can not be caused by the spike in sensor sensitivity. Note that the arrival or leaving of just one flux quantum $\Phi_0 = 20.7$ Gs μm^2, from the vicinity of a sensor of the area $A_{sen} = 25$ μm^2, may result in the jump of the measured signal of the magnitude $\Delta B \simeq \Phi_0/A_{sen} \simeq 0.8$ Gs. Therefore, we believe that the jumps indicate real sudden redistribution of flux in the vicinity of the sensor, caused by unpinning of flux from the intrinsic pinning centers. We see that the flux
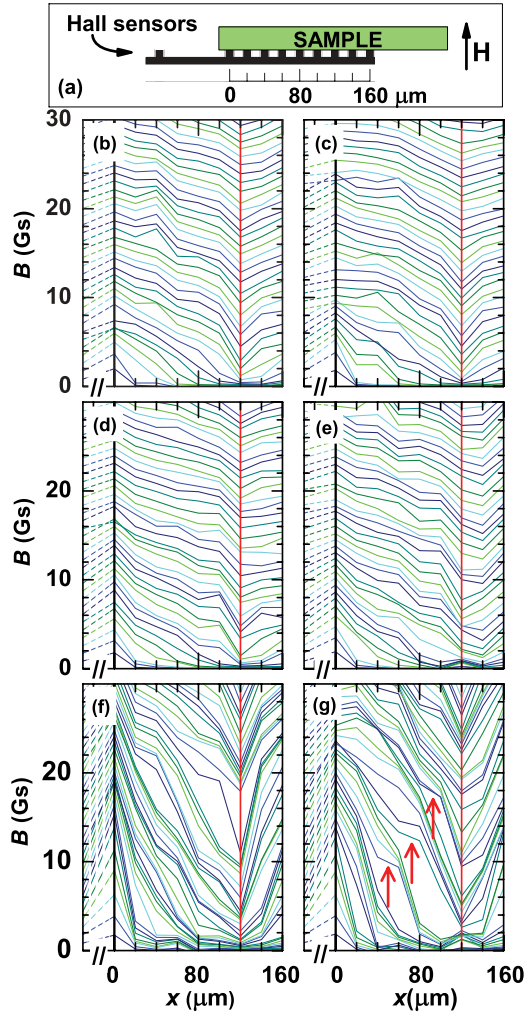
FIG. 3. (Color online) (a) Placement of the sample, with Nb adjacent to Hall sensors. (b)–(g) Flux profiles measured at $T = 7.5$ K during increasing H (shown at 1-Oe intervals) for the saturated F layers $s_+ = 0.99$ (b) and $s_- = 0.01$ (c); for negative RU domains $s_- = 0.78$ (d) and $s_- = 0.82$ (e); and for positive RU domains $s_+ = 0.22$ (f) and and $s_+ = 0.18$ (g). Vertical lines in (b)–(g) indicate, respectively, the sensor placed closest to the sample edge ($x = 0$) and closest to the middle of the sample ($x = 120$ μm). The background data, measured by the sensor residing a few millimeters away from the sample, are shown on the left vertical axis. Sensitivity of all Hall sensors is the same, about 0.05 Gs. The red arrows in (g) show the flat regions in the $B(x)$ dependence.

penetrates to the sample center at $H \approx 7$ Oe. For $H < 10$ Oe, the $B(x)$ dependence is close to the linear Bean profile,[51] but becomes slightly nonlinear as H increases, suggesting the critical current density J_c changes with increasing B. In the case of thin films, in which the thickness is much smaller than the sample width, the theories for the perpendicular configuration and field-independent critical current density predict a large nonlinear increase of $B(x)$ at the sample edge, and decrease in the sample center.[52–54] We do not see such features in our experiment. This may be related to the fact that the first sensor is positioned not exactly at the edge, but at a finite distance from it, so that rapid increase at the edge is not registered. It may also result from the finite sensor area,

which averages the signal over 5×5 μm^2, thus wiping out large nonlinearities. Finally, note that J_c is B dependent, so it is also possible that theories mentioned above do not describe the present experiment.

Figures 3(d) and 3(e) show that similar profiles are recorded when the negative RU domains are predefined, immersed in the positive (inverted) background, i.e., when $s_- = 0.78$ and 0.82. The negative RU domains repel the positively aligned vortices which enter the sample when the positive external field is increased. This repulsion has a negligible effect on the flux penetration. The similarity of these profiles to the profiles for the saturated F layer suggests that the positive vortices located above positive background do not experience any enhancement of pinning relative to the intrinsic pinning level. A reason is that the width of the background regions is large. Since the magnitude of the stray field at the domain center scales in inverse proportion to the domain width,[55] wide background regions do not create effective pinning centers for vortices. Indeed, the average distance between RU domains d may be estimated from the fact that the ratio of the surface area of RU domains to the total area is given by $s = w/(w + d)$. From this, we have $d = w(1 - s)/s$. Taking $s = 0.2$, we get $d = 1.93$ μm. On the other hand, a length scale of vortex-domain interaction is given by effective penetration depth Λ, which is equal to about 331 nm at 7.5 K, much smaller than d.

The flux profiles change dramatically for $s_+ = 0.18$ or 0.22, when the positive RU domains are predefined, immersed in a background of inverted negative domains [Figs. 3(f) and 3(g)]. Several effects are evident. First, the flux penetration is delayed so that flux appears in the sample center at $H \approx 14$ Oe. Moreover, the magnitude of B at the sample edge is strongly enhanced in comparison to the saturated F-layer case. This indicates a large accumulation of flux near the sample edge, caused by the domain pinning. The strong vortex-domain interaction is likely to be caused by the fact that w is about 460–500 nm in this case, so that it is close to $\Lambda \approx 331$ nm. Note, furthermore, that the flux profiles are not smooth. We see regions with a large slope of $B(x)$, indicative of large currents and pinned flux, intercepted by much flatter regions in which currents are low and flux is weakly pinned. The differences between slopes in these regions far exceed those observed in the case of the saturated F layer. Therefore, we are led to the conclusion that the positive RU domains trap vortices very efficiently, leading to inhomogeneous flux propagation, with areas of strongly pinned flux separated by pinning-free (or weakly pinning) areas. Since the domain patterns defined in the SFB are random, the profiles shown in Figs. 3(e) and 3(f) differ in details. Interestingly, in Fig. 3(f), we observe flat regions moving towards the sample center on increasing H, as indicated by arrows.

Highly inhomogeneous behavior of flux may be visualized by calculating directly from the data the derivative of the magnetic induction, which is proportional to the critical current density $\mu_0 J_c \approx 2dB/dx$.[56] In Fig. 4, we present contour plots of the dependencies $J_c(x,H)$, calculated from measured $B(x,H)$, for two states of the F layer with predefined positive RU domains $s_+ = 0.31$ [Figs. 4(a) and 4(b)] and $s_+ = 0.18$ [Figs. 4(c) and 4(d)]. The resolution, limited by the noise level on the sensors, is better than about 8×10^6 Am^{-2}. In each graph, the horizontal axis shows the distance across the sample
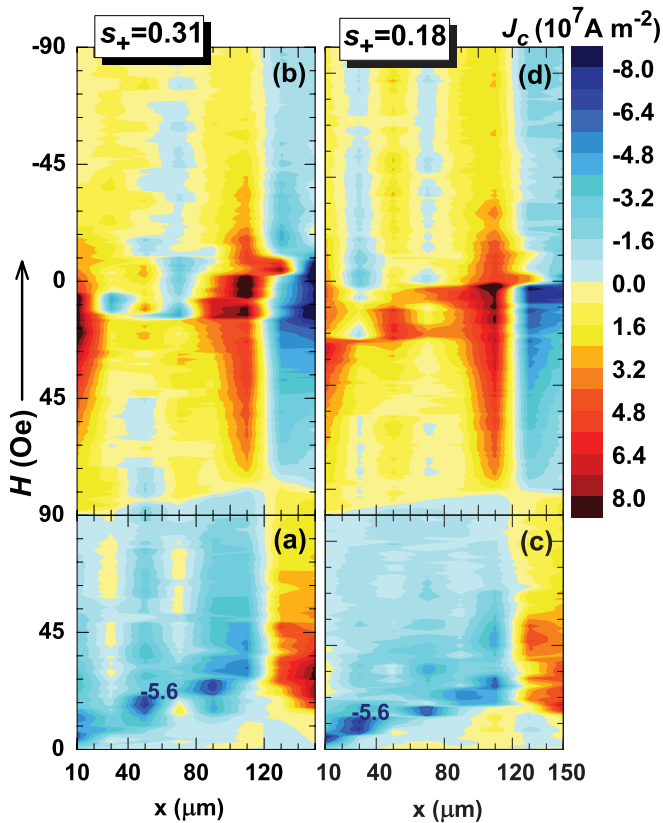
FIG. 4. (Color online) The critical current density $J_c(x,H)$ for $s_+ = 0.31$ [(a), (b)] and $s_+ = 0.18$ [(c), (d)] at $T = 7.5$ K during the H sweep from 0 to $+90$ Oe [(a) and (c)], and from $+90$ Oe to -90 Oe [(b) and (d)]. The field sweep direction is from the bottom up, as indicated by the arrow along the vertical axis. In (a) and (b), the blue line marks the level of $J_c = -5.6 \times 10^7$ Am^{-2}.

x, while the vertical axis shows the external magnetic field H, which is swept first from 0 to $+90$ Oe, and subsequently from $+90$ Oe to -90 Oe. The direction of the field sweep in the figure is from bottom up, as indicated by the arrow along the vertical axis. The first, initial part of the sweep (from 0 to $+90$ Oe) is shown in Figs. 4(a) and 4(c). During this initial sweep, J_c is negative for $0 < x < 120$ μm, consistent with the negative slope of $B(x)$ shown in Figs. 3(f) and 3(g). Subsequently, the external field is swept from $+90$ Oe to -90 Oe, and the resulting evolution of $J_c(x,H)$ is presented in Figs. 4(b) and 4(d). During this portion of the sweep, the slope of $B(x)$ becomes positive for x between the sample edge and the sample center, therefore, the sign of J_c reverses.

Figure 4 shows clearly that J_c is not uniformly distributed. In Figs. 4(a) and 4(c), which present the behavior during the initial flux penetration, we observe small "pockets" of elevated J_c, as indicated by blue contour lines drawn at the level of -5.6×10^7 Am^{-2}. This is exactly the same effect as shown by the profiles in Fig. 3(g) [i.e., regions of $B(x)$ with large slope, separated by "flat" portions]. The "pockets" are located at different x and H in Figs. 4(a) and 4(b), most likely as a result of different distribution of the RU domains for two different s values. In addition, the pockets appear at larger x as H increases, consistent with the interpretation that they signal

the motion of strongly pinned flux towards the sample center on increasing H.

The largest magnitude of J_c is observed in Figs. 4(b) and 4(d) when H approaches 0, close to the sample center (around $x = 110$ μm). The maximum J_c is about 1.32×10^8 Am^{-2} and 1.1×10^8 Am^{-2} for $s_+ = 0.18$ and 0.31, respectively, while in case of the saturated F layer, it is about 2.5 times smaller, 5.4×10^7 Am^{-2}. This enhancement of J_c by RU domains is substantially smaller than the value reached in the case of demagnetized SFBs, for which we were able to enhance J_c more than 10 times.[30] This is likely related to much smaller density of pinning centers created by RU domains in comparison with the case of demagnetized samples.

Note that in Figs. 4(b) and 4(d) there are many abrupt changes of J_c observed across the whole sample as H reaches some values. This indicates that flux does not propagate smoothly inside the sample during H sweep. The most pronounced of these changes is the rapid decrease of J_c just after it reaches the largest magnitude, when the polarity of H becomes negative. This rapid decrease signals the unpinning of positive flux from positive RU domains. In the region of negative H, much smaller values of J_c are observed because the positive RU domains repeal the negative flux.

2. Enhancement of vortex pinning

So far, we have compared the penetration of positive flux in the presence and in the absence of positive RU domains. We now proceed to assess the effect of s value on the pinning enhancement. To do this, we first predefine various s_+ and s_- states in the F layer. The inset in Fig. 5 shows the normal-state hysteresis loop measured by AHE at $T = 10$ K together with the values of s_+ and s_- for which the data shown in the main figure are taken. The main figure contains the data accumulated for s_+ [Fig. 5(a)] and s_- [Fig. 5(b)] using the sensor located at the sample center $x = 120$ μm, during the full cycle of the external field. The data are presented as a plot of the local magnetic field, which we define as $H_{loc} = B - \mu_0 H$, versus external field. As we can see, these plots resemble hysteresis loops usually measured by global magnetization measurements.

The innermost loops in Figs. 5(a) and 5(b) show the data for the saturated F layer. These curves are smooth, and loops are symmetric with respect to the polarity of H. Also, the ascending and descending branches of the loop show approximately the same magnitude of H_{loc} value, confirming that the intrinsic pinning in our film is of bulk nature, i.e., no unusual surface or edge barriers exist for the flux penetration, of the type discovered and studied extensively in high-temperature superconductors.[57]

When the RU domains are defined in the F layer, the peak-to-peak width of the hysteresis loops increases, the loops cease to be smooth, and they become asymmetric with respect to the polarity of H. All these effects are strongly s dependent and become most pronounced when s_+ decreases below 0.3 or s_- increases above 0.7, that is, when the width of RU domains defined in the F layer becomes small. The examples of such strongly asymmetric loops are shown in Fig. 5(a) for $s_+ = 0.22$ and $s_+ = 0.18$, and in Fig. 5(b) for $s_- = 0.78$ and $s_- = 0.82$. The width of hysteresis loop is seen to increase strongly
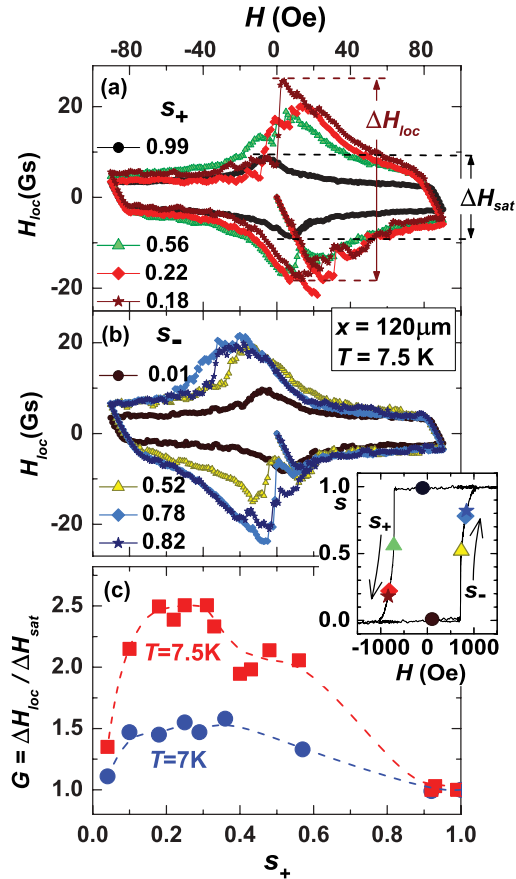
FIG. 5. (Color online) Hysteresis loop of H_{loc} measured at $x = 120$ μm and $T = 7.5$ K for various s_+ (a) and s_- (b). For clarity, only some of the s values are shown. Inset: Hysteresis loop of Co/Pt measured by AHE at 10 K (line); points show the s values for which the data shown in the main figure are taken (color and shape coded to match main figure). (c) The enhancement of pinning $G = \Delta H_{loc}/\Delta H_{sat}$ versus s_+. The definitions of ΔH_{loc} and ΔH_{sat} are shown in (a).

when the polarity of H is the same as the polarity of RU domains (positive H in s_+ case and negative H in s_- case). On the other hand, when the polarity of H is opposite to that of RU domains, the width of the loop is very close to that measured in the saturated F layer. This confirms the picture inferred from $B(x,H)$ and $J(x,H)$ dependencies presented in Figs. 3 and 4. The polarity-dependent asymmetry is precisely what is expected in the case of magnetic pinning of vortices by RU domains.[11–13,22,23,28,30] Note that both the enhanced width of the hysteresis loop and the asymmetry decrease when the magnetic reversal process is less advanced, so that s_+ is larger than 0.3 or s_- is smaller than 0.7. Examples are two hysteresis loops measured for $s_+ = 0.56$ [Fig. 5(a)] and $s_- = 0.52$ [Fig. 5(b)]. In these cases, the MFM images show that w exceeds 550 nm, and the RU domains are multiply interconnected. While the first factor decreases the domain-vortex interaction, the second creates channels for vortex flow, and both may contribute to the decrease of magnetic pinning.

While we can extract the full $J(x,H)$ dependence from the data, the simpler and equally valid procedure of assessing the influence of s on the pinning is the estimation of the

peak-to-peak width of the hysteresis loop ΔH_{loc}, and a comparison to a similar quantity for the saturated F layer ΔH_{sat} [these definitions are illustrated in Fig. 5(a)]. This is because B, measured by the central sensor, is proportional to dB/dx integrated over x from the sample edge to the sample center. Therefore, $\Delta H_{loc}/2$ provides an approximate estimate of the density of flux pinned inside the sample from the edge to the center, averaged over the bottom and top branches of the hysteresis loop. The pinning enhancement is then given by the ratio $G = \Delta H_{loc}/\Delta H_{sat}$, which is displayed versus s_+ in Fig. 5(c) for two different temperatures.

We see that the largest enhancement of pinning occurs in the range of s_+ values from about 0.15 to 0.35. It reaches about 2.5, exactly the same value as the estimate we have obtained from $J_c(x,H)$ dependencies. Beyond the range $0.15 < s_+ < 0.35$, the domains pin vortices less efficiently. While at low s_+ this is most likely caused by a small total area of the RU domains, at large s_+ the increasing widths of RU domains and domain interconnections presumably reduce the pinning.

Another interesting effect seen in Fig. 5(c) is the decrease of the domain-induced pinning enhancement with the decreasing temperature. We see that G decreases to about 1.5 on lowering T to 7 K. This is most likely caused by a different T dependence of intrinsic and magnetic pinning. At $T = 7.5$ K, the intrinsic pinning is very weak, presumably because the coherence length greatly exceeds the size of intrinsic defects providing the pinning. On lowering T to 7 K, we observe rapid increase of intrinsic pinning, as evidenced by the increase of ΔH_{sat} by a factor of about 1.9. It follows that in the same T range, the magnetic pinning increases by a smaller factor, of about 1.2. The weaker dependence of the magnetic pinning on T may be caused by the fact that the vortex-domain interaction depends on the relative size of Λ and w, which are of the same order of magnitude at these temperatures. Later, we will discuss some other factors which may influence this T dependence.

As we have already mentioned, the hysteresis loops measured for SFB with predefined RU domains are not smooth, in sharp contrast to the case of the saturated F layer. As H is ramped, we observe the appearance of many sudden changes of H_{loc}. These jumps are the most pronounced when the enhancement of pinning and the asymmetry of the loops are the largest. Both the magnitude of the jumps and the fields at which they occur are somewhat random; that is, if the H cycle is repeated, they may be slightly altered. However, most of the jumps are definitely much larger than ± 1 Gs, so we may conclude that they reflect a real sudden change of flux in the sensor area.

Interestingly, some regularity and reproducibility in the jumps appearance is noted. In order to explain this, we focus on the positive RU domains $s_+ = 0.18$ case [Fig. 5(a)], and compare the top and bottom branches of the hysteresis loop in the range of positive H (when pinning on RU domains is strong). We observe many flux jumps, not exceeding about 4 Gs, on the bottom branch of the loop, i.e., during the flux entry into the sample. On the other hand, the top branch appears to be slightly more smooth. However, a single exceptionally large flux jump, about 18 Gs, occurs in the vicinity of $H = 0$, i.e., in the final stage of the positive flux expulsion from the sample. This large jump is the same event as the one already visualized

in Fig. 4(d) by the sudden decrease of J_c around $H = 0$. A similar picture is seen for negative RU domains $s_- = 0.78$ [Fig. 5(b)] in the range of negative H. In this case, many small jumps are seen at the top branch, during the flux entry, while a bottom branch is somewhat more smooth but shows a large jump around $H = 0$ in the final stage of negative flux exit. While repeating the same hysteresis loop may produce a large jump with somewhat altered magnitude and sharpness, it is always observed. The jump exists also for other s values, but with smaller magnitude and sharpness. These observations may be summarized as follows. When the polarity of the RU domains and the external field are the same, the flux entrance into the sample is not smooth, but follows a series of small jumps. This suggests strong pinning by RU domains, possibly even some commensurability on a local scale. On the other hand, when H decreases, the flux remains strongly pinned until at $H \approx 0$ a sudden unpinning event occurs, and a large density of vortices leaves the sample center.

Finally, we note that the appearance of sudden changes of H_{loc} is not at all surprising in the system with discrete pinning centers. The jumps in magnetization have been observed before, for example, in the Pb film on the top of an array of magnetic dots.[58] In this case, the change of the polarity of H with respect to the magnetic moment of the dots induces flux expulsion very similar to the one observed in our experiment.

3. Flux confinement during the initial flux entry

While the data presented in Fig. 5(c) give some qualitative information about s dependence of the magnetic pinning, they are quite scattered because of the presence of flux jumps, which occur as a result of complicated interplay of vortex-domain and vortex-vortex interactions. It is not possible to reach any quantitative conclusion about the role of magnetic-domain geometry on the pinning process based on these data.

Instead, we turn the attention to the initial stage of flux penetration process, when the density of flux inside the sample is relatively low, and flux jumps do not affect the behavior so strongly. In Fig. 6, we plot $B(H)$ and $H_{loc}(H)$ dependencies measured for small H for the saturated F layers $s_+ = 0.99$ [Figs. 6(a) and 6(b)] and for $s_+ = 0.22$ [Figs. 6(c) and 6(d)]. The data are taken by several sensors situated at consecutive positions inside the sample, beginning from the sensor closest to the edge ($x = 0$) and ending with sensor closest to the sample center ($x = 120$ μm).

We consider first the curves measured at the sample center ($x = 120$ μm). They are very similar to what is usually measured by global magnetization measurements, i.e., we see a delayed penetration of flux in the sample center, evidenced by $B(H)$ deviating from zero. This occurs at $H \approx 7$ Oe for $s_+ = 0.99$ and at $H \approx 14$ Oe for $s_+ = 0.22$. Simultaneously, $H_{loc}(H)$ deviates from a straight line which marks the Meissner region, and this is further followed by a broad minimum and the increase of H_{loc} signaling the appearance of large flux density pinned inside the sample. In the presence of RU domains, the shape of the minimum and the following growth of the flux density are not smooth, but show jumps when sudden unpinning events influence the flux penetration. As we now look at data measured by sensors at smaller x, we observe that the minimum on the $H_{loc}(H)$ curve shifts towards smaller
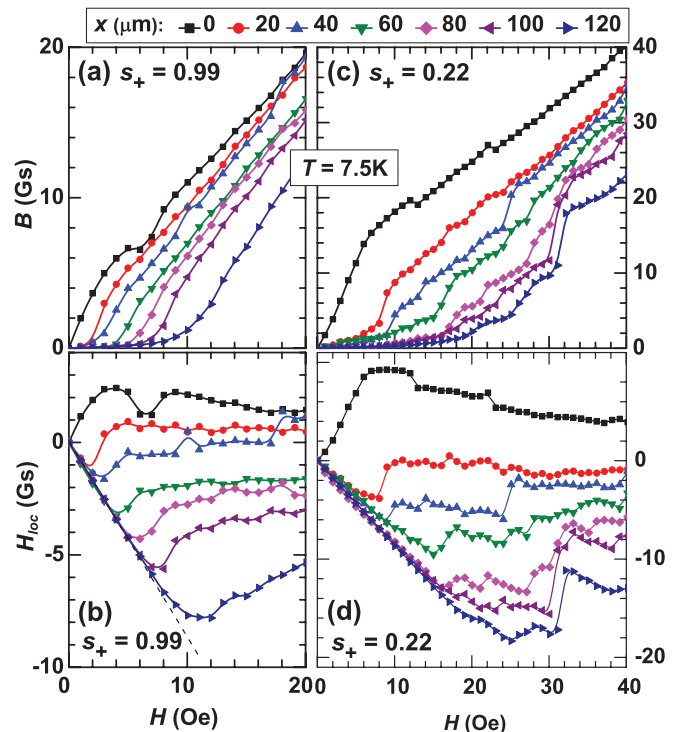

FIG. 6. (Color online) $B(H)$ [(a) and (b)] and $H_{loc}(H)$ [(c) and (d)] versus H at various sensor positions x, measured at $T = 7.5$ K for the saturated F layer [(a) and (c)], and for $s_+ = 0.22$ [(b) and (d)]. All lines are guides to the eye.

H with decreasing x, indicating that the flux front arrives at these positions at smaller H. Again, in the case of $s_+ = 0.22$, the shapes of the minima are slightly different at each x as a result of domain-induced pinning, taking sometimes a form of slow deviation from a Meissner linear behavior followed by a sharp jump. Nevertheless, we see clearly that in the case of $s_+ = 0.22$, the flux front arrives at any given x at larger H than in the case of the saturated F layer.

The most interesting are the data taken by the first sensor, closest to the sample edge. They show no minimum at all, which tells us that the flux front passes this sensor at very small field, below the first step in our measurements (1 Oe). Therefore, the first sensor is situated in the flux penetrated region and we can extract the average vortex density in this region n from the magnetic induction measured by the first sensor $n = B/\Phi_0$.

We note further that the $B(H)$ curve measured by the first sensor shows a change of slope at certain $H = H_0$, indicating that the growth of B with increasing H slows down at H_0. In the case of $s_+ = 0.22$, this change is very well defined and occurs at $H_0 \approx 8$ Oe, while in $s_+ = 0.99$, it is somewhat less obvious, but may be placed at $H_0 \approx 3.5$ Oe. This slowing down is much better visible on the $H_{loc}(H)$ curve, where it takes a form of a maximum at the same value of H_0. This is because for $H \lesssim H_0$, the density of flux measured by the first sensor is growing faster than H, while for $H \gtrsim H_0$ it is growing slower than H. Most interestingly, in close vicinity of the same H_0, we observe a large jump in the flux density measured by the second sensor at $x = 20$ μm. This clearly indicates that slowing down of the increase of B, measured

by the first sensor, is associated with the transfer of flux further inside the sample. We therefore interpret the maximum of H_{loc} as an evidence that for $H \lesssim H_0$, the flux is accumulated in the region of the first sensor, while for $H \gtrsim H_0$ it starts to transfer towards inside the sample. The magnitude of the accumulated flux density, just before it starts to transfer, may then be estimated from the value of B at $H = H_0$. Note that $B(H_0)$ is only about 6 Gs in the case of $s_+ = 0.99$, but it is much larger, about 16 Gs, in the case of $s_+ = 0.22$. This clearly points to the enhancement of the flux accumulation induced by RU domains.

A similar change of slope of $B(H)$ in the initial stages of the flux propagation has been observed before, most recently in case of thin Pb film with periodic pinning array.[45] This feature is usually attributed to demagnetization effects which lead to compression of flux lines close to a border of thin film placed in perpendicular magnetic field.[54] While in the case of the F-saturated sample this feature is weak, it is strongly enhanced in the presence of magnetic pinning in the $s_+ = 0.22$ case. One may expect that the demagnetization effects are affected by enhanced critical current density or that the magnetic pinning directly influences the change of slope by trapping of vortices or, most likely, both. No theory exists yet which would describe these effects in the presence of strongly inhomogeneous critical current density. However, independent of detail mechanism, the ultimate source of this effect is the presence of RU domains which pin vortices, and from our experiment we can directly extract the enhanced vortex density in the flux penetrated region.

Since the change of slope of $B(H)$ is easier to identify in the $H_{loc}(H)$ dependence, we display in Fig. 7 a collection of $H_{loc}(H)$ curves for various s_+ and s_- measured at $T = 7.5$ K at $x = 0$. All curves show a maximum at some external field $H = H_0$, followed by a decrease when the v-v interactions force vortices to leak away towards the sample center. The decrease of H_{loc} is not smooth: there are sudden jumps (up or down) of the height between 0.7 to 2.5 Gs, which indicate the

change (increase or decrease) of the vortex density probed by the first sensor $\delta n = \delta H_{loc}/\Phi_0$.

Both H_0 and $H_{loc}(H_0)$ are dependent on s. In the case of the saturated F layer, $H_{loc}(H_0)$ is about 2.5 Gs, and it becomes much larger in the s_+ process, particularly for s_+ below 0.6, i.e., when the positive RU domains become abundant, reaching the largest magnitude at $s_+ \approx 0.22$. This is a clear indication that the effect is caused by RU domain-induced pinning. This is further confirmed by the behavior observed in the s_- process. In this case, no increase of $H_{loc}(H_0)$ is seen in the second half of the reversal process, for $s_- > 0.5$, when large amounts of negative RU domains are present because negative RU domains repel positive vortices. On the other hand, small enhancement appears in the first half of the reversal, when $s_- = 0.03$ or 0.44. This is because freshly inverted positive domains of small dimensions pin positive vortices.

From the maxima of H_{loc}, we obtain the corresponding density of vortices $n = B(H_0)/\Phi_0 = [H_{loc}(H_0) + \mu_0 H_0]/\Phi_0$. This is the density of vortices which is accumulated in the vicinity of the first sensor, before the v-v interactions push them towards the sample center. We would like to emphasize that the quantity n is not the absolute maximum of the flux density which exists in this area because that one is continuously increasing with increasing external field. Instead, n gives us a snapshot of the flux density at $H = H_0$, when the density of *trapped* flux, measured by H_{loc}, reaches maximum.

Figure 8(a) shows $n(s)$ for the s_+ process, measured at three temperatures $T = 6.5$, 7, and 7.5 K, and for s in the range from 0.03 to 0.6, when domain-induced pinning is strong. The scatter of the data reflects the fact that the domain patterns are random. Nevertheless, the data may be extracted with good accuracy because the initial entry of flux into the vicinity of the first sensor does not suffer flux jumps. The jumps only start to appear when the flux exits the area. This is reasonable because during the flux entry there are few vortices present so they are mainly subject to strong magnetic pinning and demagnetization effects, which both prevent vortices from leaving the area of the first sensor, while the repulsive v-v interactions remain relatively small. This results in a smooth increase of the density of trapped flux. Eventually, when the flux density becomes large, the repulsive v-v interactions overcome the remaining interactions leading to flux propagation. In the presence of random magnetic pinning potential, this propagation is strongly nonuniform, with many flux jumps.

In Fig. 8(a), two effects are evident. First, the shape of the $n(s)$ dependence is similar for all temperatures, with rapid increase at small s, and two wide maxima separated by a shallow minimum, situated at $s \approx 0.25$. While the dependencies for $s \lesssim 0.35$ are quite well defined, for larger s they show more variability. This may reflect the fact that the magnetic-domain landscape in this region of s is more disordered, with much larger dispersion of domain width, which may lead to larger fluctuation of n measured by a small sensor. This may also indicate that the mechanism of magnetic pinning is somehow different in the small-s and large-s regions. The shape of $n(s)$ resembles somewhat the $G(s)$ dependence, but differs in details. This is because G describes the enhancement of flux pinning inside the whole sample, from the edge to the center, and in the presence of large
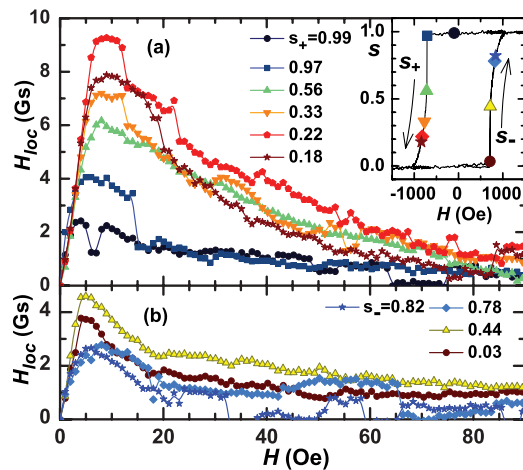

FIG. 7. (Color online) H_{loc} versus H at $x = 0$ and $T = 7.5$ K for various s_+ (top) and s_- (bottom). For clarity, only some of the s values are shown. Inset: Hysteresis loop of Co/Pt measured by AHE at 10 K (line). Points show the s values for which the data shown in the main figure are taken (color and shape coded to match main figure).
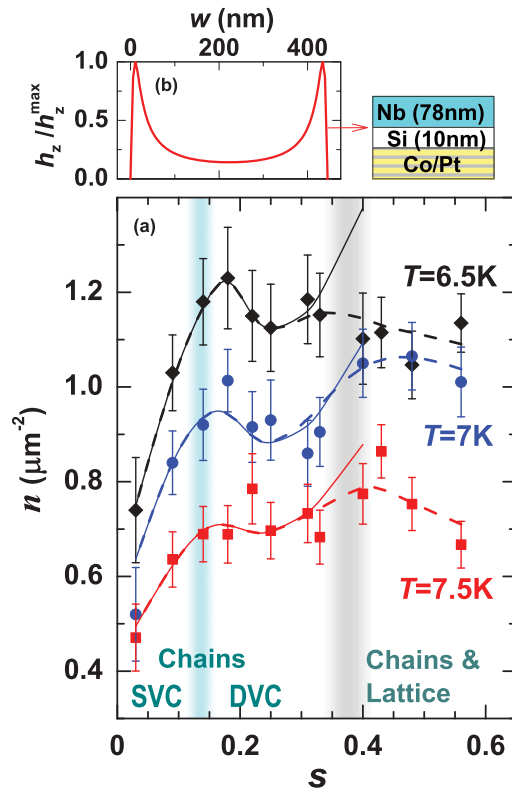
FIG. 8. (Color online) (a) n versus s in the s_+ process, at $T = 7.5$ K (squares), 7 K (circles), and 6.5 K (diamonds). Continuous and dashed lines through points: fits to the models described in the text. The labels SVC and DVC mark regions of vortex confinement into single and double vortex chains, respectively; vertical shaded bands indicate two transition regions: between SVC and DVC regions (blue band), and between "chains" and "chains and lattice" regions (gray band), as discussed in the text. (b) Perpendicular component of the stray magnetic field normalized to maximal value h_z/h_z^{max} at the Nb surface adjacent to the Si buffer layer.

flux density (subject to flux jumps), so it can not be expected to show exactly the same behavior as n. However, the initial rapid increase of n at small s is similar to what is observed in $G(s)$, and this is most likely caused by the rapid increase of the RU domain area, as shown by MFM data. On the other hand, the nonmonotonic behavior of n for $s > 0.17$ is more difficult to explain since both w and L change monotonically with s. In the following section, we will discuss this dependence in more detail, and we will explain the labels shown in the figure, as well as the meaning of the shaded (blue and gray) bands drawn in the figure.

The second effect observed in Fig. 8(a) is a definite increase of n with the decrease of temperature in the region of $s \lesssim 0.35$. Again, at $s \gtrsim 0.35$, the behavior seems to be more complicated, with the initial increase of n on cooling from 7.5 to 7 K, followed by weaker change on further cooling; however, this conclusion is less certain because of larger disorder of the domain pattern in this region. In any case, these results suggest that the magnetic pinning increases when T is lowered. In particular, n increases by a factor of 1.3 on lowering of T from 7.5 to 7 K, which agrees well with the estimate of the increase

of magnetic pinning by a factor of 1.2 obtained from the $G(T)$ dependence [Fig. 5(c)].

C. Discussion and modeling of the vortex confinement

We start our discussion from the comment on the inhomogeneous flux penetration illustrated by Figs. 3 to 5. Various examples of the irregular flux penetration have been reported in the past. The scanning Hall microscopy of Pb film with periodic antidot array has revealed the terraced critical state in the initial stages of the flux penetration,[45] predicted first by Cooley and Grishin,[46] and more complex penetration at higher fields, as suggested by the numerical simulations by Reichhardt *et al.*[47] In such systems, the irregular flux behavior originates from commensurability between the vortex lattice and the underlying pinning arrays. When the pinning arrays are disordered, the matching effects are modified, however, they do not disappear completely. This has been shown by magnetoresistance studies of Nb films with quasiperiodic magnetic pinning arrays.[5] In this experiment, the commensurability occurs on a local scale in spatially limited areas of sample, still, matching effects could be observed, although they result in a nonperiodic series of magnetoresistance minima. Taking one step further, we may expect that in even more disordered systems the commensurability may survive on a local scale, although long-range matching effects would not be present. Since our measurements are local, we believe that our results may be interpreted as an indication of matching effects which occur on a local scale.

An interesting observation is the weak increase of the magnetic pinning with decreasing temperature. This increase does not necessarily imply that the interaction between single vortex and RU domain increases. The strength of the magnetic interaction roughly depends on the ratio of its range, given approximately by Λ, to the domain width w. In the present experiment, we have $\Lambda \lesssim w$. For example, when $s = 0.17$ [the approximate position of first maximum in $n(s)$], $w = 445$ nm, so that Λ/w is reduced from 0.74 to 0.53 on lowering of T from 7.5 to 7 K. In this case, the strength of interaction depends crucially on the spatial profile of the stray magnetic field generated by the domain. This is illustrated in Fig. 8(b), where we plot the profile at the side of Nb layer adjacent to the Si buffer, calculated using the equations from Ref. 55 for $w = 445$ nm. We see that the maximum stray field is close to the domain boundaries. Therefore, we may expect that the vortex-domain interaction is the strongest for the large Λ/w (at $T = 7.5$ K), and it is reduced when Λ/w decreases with decreasing T. We conclude that the increase of magnetic pinning on lowering of T most likely can not be attributed to the increase of interaction between single vortex and magnetic domain. Instead, a more complicated process may be involved, for example, some type of matching effects, or confinement effects, which become stronger as T decreases.

Another intriguing question is the origin of $n(s)$ dependence observed in the initial stage of the flux penetration in the vicinity of the sample edge. The smooth initial increase of $B(x)$ (below H_0) suggests that the vortices fill up potential minima produced by the combined effects of magnetic pinning, self-field, and v-v interactions. It is worth to mention in this context that in the case of the antidot array on Pb film mentioned

above, it has been observed that vortices progressively fill up the rows of antidots at the beginning of flux penetration.[45] In the present case, the potential minima are located in the regions of RU domains, so it is reasonable to assume that these pinning centers will be occupied first. In the following, we therefore consider a possible arrangement of vortices confined to RU domains, which could be compatible with the observed $n(s)$ dependence.

We restrict our considerations to the two simplest arrangements. One possibility is that the vortices pinned by neighboring RU domains are correlated and form the Abrikosov vortex lattice. In the presence of the random magnetic-domain pattern, the lattice is distorted and correlations occur on a local scale, similar to the quasiperiodic magnetic pinning arrays.[5] However, when the distances between RU domains are large (as in the small-s range), the vortices pinned by neighboring RU domains may not be correlated. The alternative picture for the small-s region is that the confinement to RU domains leads to correlation *within* each RU domain area, thus leading to formation of various vortex chains pinned above RU domains. Recently, the confinement of vortices to chains above domains of one sign has been directly observed by STM imaging of a NbSe$_2$/permalloy bilayer with the ordered stripe domains.[27] While at high $H \gtrsim 200$ Oe some vortices appear beyond the boundaries of the domains of one sign, at low H they reside exclusively within these domains. We have reached a similar conclusion by the analysis of the magnetoresistance measurements performed on SFBs similar to the present sample, but with quasiordered magnetic domains of tunable width defined by angled demagnetization.[28] We have found that the activation energy for vortex pinning exhibits maxima at matching fields when two distinct vortex patterns are formed within magnetic domains of one sign, single vortex chains (SVC), or double vortex chains (DVC), as depicted in Fig. 9(b). The SVCs, with the v-v distance a, are formed for small w. When w increases, the v-v repulsion tends to push vortices further away from each other, so that the DVC pattern may be formed, with chain separation by a distance $h < w$. In that case, the v-v distance a is given by $a^2 = (b/2)^2 + h^2$, where b is the v-v separation along each chain. The DVCs appear first when w exceeds the boundary value of $w_D = 0.389$ μm. At $w \simeq w_D$, SVC and DVC coexist, and in this case we have estimated the interchain distance $h \approx 0.6w$.

Vortex lattice. To examine the hypothesis of the lattice formation, we first use the data from Fig. 8(a) to calculate the average lattice constants a_L for the triangular lattice with the vortex density n, $a_L^2 = (4/3)^{1/2}/n$. They are displayed by open points in Fig. 9(a) as a function of s for different temperatures. Next, we check if these values of a_L are compatible with the geometry of the magnetic-domain pattern. To do this, suppose for a moment that we have defined a pattern of regular stripe magnetic domains with the width w and the distance between domains d. In this case, the perfect triangular lattice with the lattice constant a_{Lg} may be formed when $a_{Lg} = 2(d + w)/\sqrt{3}$. Substituting the relation $d = w(1 - s)/s$, we get the requirement for the lattice constant imposed by domain geometry $a_{Lg} = 2w/(\sqrt{3}s)$. However, since in the present experiment we deal with the random magnetic-domain pattern, with average domain width w and standard deviation Δw, we expect the above requirement to vary on a local scale.
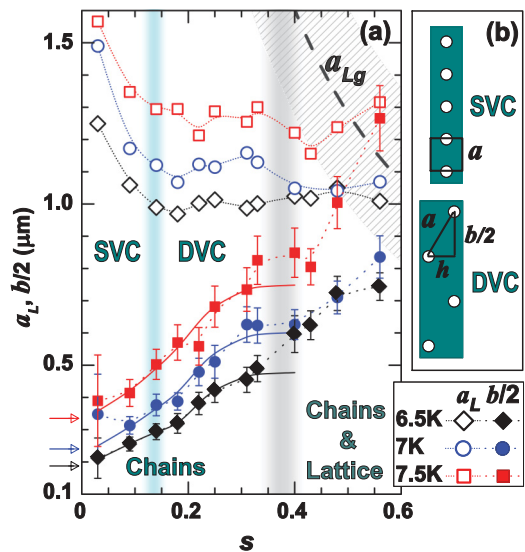

FIG. 9. (Color online) (a) The dependence on s of the Abrikosov lattice constant a_L (open points) and the v-v distance along the chains $b/2$ (full points), extracted from n, at $T = 7.5$ K (squares), 7 K (circles), and 6.5 K (diamonds). The thick dashed line marked "a_{Lg}" and the hatched area indicate the average Abrikosov lattice constant and its standard deviation, respectively, allowed by the domain geometry. All dotted lines are guides to the eye, thin continuous lines are fits to the model described in the text, and vertical shaded bands indicate two transition regions, defined in the text. The arrows on the left indicate values of Λ at 7.5, 7, and 6.5 K (from the top down). (b) Schematic vortex patterns: single vortex chain (SVC, top) and double vortex chain (DVC, bottom).

Therefore, it should be replaced by a condition which allows a range of possible lattice constants, with average value a_{Lg} and standard deviation Δa_{Lg} corresponding to the respective values of w and Δw. In Fig. 9(a), the average a_{Lg} is shown by a thick dashed line, and the standard deviation Δa_{Lg} is marked by the hatched area. We see that the hatched area is situated in the large-s region, where it overlaps with a_L data extracted from n. This indicates that the formation of triangular lattice is possible for large s, at least locally, in some areas of the sample. This occurs because the distances between domains are comparable to the domain width, so that the vortices pinned by neighboring domains may be correlated.

On the other hand, as s decreases below about 0.35–0.4, the hatched area strongly deviates from the data of a_L extracted from n. In Fig. 9(a), we draw a vertical shaded (gray) band in a region where the deviation occurs. The deviation stems from the fact that d greatly exceeds w at small s. Thus, for $s \lesssim 0.35$, the lattice can not be formed unless some "interstitial" vortices are pinned between RU domains by v-v interactions. This type of behavior, termed "caging" of vortices, has indeed been observed in the case of periodic magnetic dot arrays at higher magnetic fields when v-v interactions become strong.[10,59,60] However, unlike in the case of magnetic dot arrays, in the SFBs the background between RU domains is formed by wide domains of opposite sign, which are (weakly) antipinning and strongly interconnected. Therefore, caging of vortices does not seem to be very likely, particularly in the initial stage of flux penetration.

Vortex chains. The preferential chain pinning by RU domains is an attractive explanation of our results for two reasons. At small s, the domains take the shape of a narrow long strips, with uniform small width w, and we have shown in our previous work that magnetic pinning becomes particularly strong when the width of magnetic domains is small, comparable to the penetration depth.[30] In addition, the T dependence of $n(s)$ is particularly easy to explain. This is because Λ decreases with the decrease of T, and a larger density of vortices may be confined by the magnetic domains of approximately the same width.

To examine the plausibility of the chain formation, we calculate the v-v distances in the vortex chain patterns using the experimental data shown in Fig. 8(a). To explain the procedure, we first note that n is an average vortex density measured by the sensor of the area $A_{sen} = 5 \times 5\ \mu m^2$. If the vortices are actually confined to the area of RU domain, which is given (from MFM measurement) by sf_A, then the signal measured by the sensor originates from a much smaller area, given by $A_{sen}sf_A$. Therefore, if the real density of vortices confined to domain is larger than n, it is given by $n/(sf_A)$. The exception may be expected for the case of a very small s, when the domain-induced pinning is weak and the term due to the intrinsic pinning n_0 is comparable to the density of vortices pinned by domains. The simplest method to take this into account is to subtract n_0 from n, so that the density of vortices confined to domains would be given by $(n - n_0)/(sf_A)$. We do this for the smallest s, $s = 0.03$. The term n_0 is estimated from several measurements for $s \approx 0$ (this procedure increases experimental error for $s = 0.03$).

We now consider vortex patterns as depicted in Fig. 9(b). In the DVC pattern, the average area per vortex is $bw/2$, so that vortex density is $2/bw$. From the equation $n/(sf_A) = 2/bw$ it follows that b is given by $b = 2sf_A/(nw)$. This formula is also valid for the SVC pattern, for which $h = 0$ so that $b/2 = a$. We also mention that the formation of triple vortex chains has been reported, but this occurs for larger domain widths and at larger magnetic fields than those used in the present experiment,[27] so we do not consider such patterns.

The dependence of $b/2$ on s for different temperatures is displayed in Fig. 9(a) by full points. We emphasize that these are the points calculated straight from experimental values of n; the only assumption is the formation of vortex chain pattern. The boundary between SVC and DVC is likely to occur in the vicinity of $w_D = 0.389\ \mu m$, as found in our previous work,[28] which in the present case is at $s \approx 0.13$. We mark this boundary by the shaded vertical (blue) band. We see that at small s, the confinement of vortices to domains leads to v-v distances a $(=b/2)$ substantially smaller than a_L. These values are just slightly larger than the respective values of Λ, shown by arrows on the left side of Fig. 9(a). This close correspondence indicates that vortices may be very closely packed above the narrow domains. Similar close packing of vortices in the chain patterns has been observed by STM in NbSe$_2$/permalloy bilayers.[27] This gives us confidence that the proposed flux confinement into chain structures may indeed occur. On the other hand, with increasing s the confinement is relaxed, until eventually, at large s, $b/2$ approaches a_L. This again confirms that in the large-s region, the conditions are favorable for the formation of the Abrikosov lattice. Since the

domain patterns in our samples are random, it is quite likely that this happens only in limited areas, while in other areas chains may still persist. Accordingly, we label small-s and large-s regions as "chains" and "chains and lattice" regions.

Searching for the possible origin of a well-defined first maximum in $n(s)$ dependence at $s \approx 0.17$, we observe that it is reflected in the dependence of $b/2$ on s as a slight upward change of slope at $s \approx 0.17$, best seen for the data taken at $T = 6.5$ K. The possible origin of this effect may be the rapid increase of the domain length L found by MFM [see Fig. 1(d)], which contributes to the faster increase of b at $s \gtrsim 0.17$. The increase of L leads to increasing interconnection of RU domains and thus allows vortices to flow easier along domains. We conclude that $n(s)$ dependence most likely results from the interplay of two factors: (1) the growth of the total RU domain area with increasing s, that pins more vortices, and (2) the simultaneous increase of w and the related exponential growth of L that relaxes the confinement. While the first factor prevails for small s, the second factor becomes dominating when L grows rapidly.

Finally, in addition to the distance $b/2$, which is calculated straight from measured n values, we can also extract the distance a, which in the DVC pattern is larger than $b/2$. For this we assume the boundary between SVC and DVC at w_D and the chain separation $h = 0.6w$, as we have found previously for similar SFBs.[28] Since at w_D SVC and DVC patterns coexist, for the data point closest to w_D we take an average of the a values for SVC and DVC.

The resulting $a(s)$ dependence (not shown here) does not exhibit the bend of slope at $s \approx 0.17$ which is seen in $b/2$. This stems from the fact that a depends both on b, and, via h, on w. In fact, we find that in the chain region ($s \leqslant 0.3$), the relation between a and w is well described by a simple power-law function $a = a_0 + \alpha(w - w_0)^\beta$, where $w_0 = 0.28\ \mu m$ is the minimal value of w observed in our sample. This is depicted in Fig. 10 where we plot a versus $w - w_0$ for $s \leqslant 0.3$ for the three temperatures. The continuous lines show the power law fitted to the data. The best fit is achieved for $T = 6.5$ K, with the exponent $\beta = 1.33 \pm 0.01$. Fits for higher T's give a similar exponent, but they are less accurate because of larger data scatter. To keep this analysis as simple as possible, we fix the exponent at the value of 1.33 for higher T's. From the fits we obtain the minimal v-v distances in the chains a_0 equal to 199 ± 5, 240 ± 20, and 347 ± 29 nm for $T = 6.5$, 7, and 7.5 K, respectively, slightly larger than the respective values of Λ. (The respective values of the α parameter are 2.08, 2.43, and 2.56, with an accuracy better than 10%.)

We believe that this robust power-law dependence of a on w reflects the fact that in the chain region it is the width of magnetic domains which provides the confinement of vortices into chains. More insight may probably be gained by numerical simulations of the vortex-domain structure, similar to simulations described in Refs. 27 and 61, but this is beyond the scope of this paper.

Using the fitted power-law dependence for $a(w)$, we recalculate the dependencies $b/2(s)$ and $n(s)$. They are plotted by the continuous lines in Figs. 9(a) and 8(a), respectively. We see that the lines describe very well the data in the chain region, reproducing the maximum in n and the change of slope in $b/2$ at $s \approx 0.17$. On the other hand, the lines calculated from
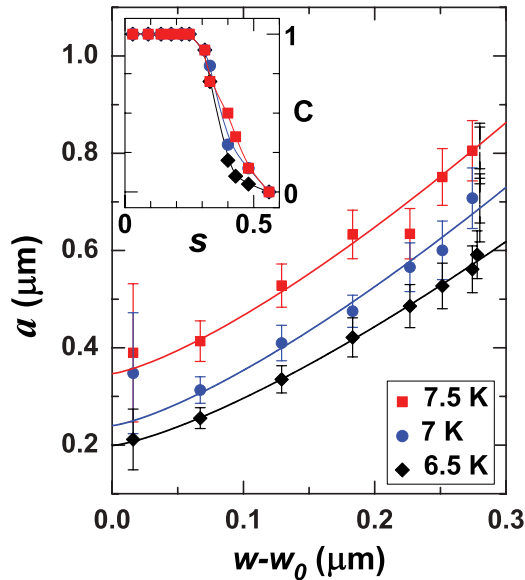
FIG. 10. (Color online) a versus $w - w_0$ in the chains region ($s < 0.3$), at $T = 7.5$ K (squares), 7 K (circles), and 6.5 K (diamonds). Continuous lines: Fits to power-law dependence. Inset: C (chain contribution to the total vortex density) versus s.

the power-law dependence deviate from the data for $s > 0.3$, showing clearly that the chain confinement does not describe the results in the chain lattice region.

The proper description of the chain and lattice region for $s > 0.3$ would be rather complicated. However, we can use a simple model to account for the observed behavior. We assume that the total density of vortices confined to domains in this region n is a sum of chain (n_{ch}) and lattice (n_L) contributions, $n = Cn_{ch} + (1 - C)n_L$, with the constant C describing the magnitude of the chain part. We take n_{ch} equal to that obtained from the fitted power-law dependence $a(w)$, shown by continuous lines in Fig. 8(a). To estimate n_L, we use the average a_L data for the Abrikosov lattice constant for s between 0.5 and 0.6 [shown in Fig. 9(a)]. We then fit the value of C separately for three different temperatures to obtain the best description of the total n. The inset in Fig. 10 shows the resulting C values versus s. We see that the decrease of chain contribution C from 1 to 0 occurs gradually for s in the range

0.3 to 0.6, and the decrease is similar for all temperatures. The dashed lines in Fig. 8(a) show the resulting total n, which is seen to describe the data quite well, despite the simplicity of this model. This gives support to the picture in which a random mixture of different areas exists, with vortices confined to chains in some areas, while in other areas the Abrikosov vortex lattice is formed.

IV. CONCLUSIONS

In this work, we have studied the influence of the magnetic-domain patterns on the vortex confinement in a single tunable planar SFB with the F layer with perpendicular magnetic anisotropy. Using a line of miniature Hall sensors, we observe the trapping of vortices by the magnetic domains in the vicinity of the sample edge, and nonuniform flux penetration into the sample. The magnetic domains enhance the pinning of vortices leading to nonuniform distribution of the critical current density. The lowering of temperature results in the weak increase of the magnetic pinning, substantially weaker than that of the intrinsic pinning. These effects strongly depend on the magnetic-domain geometry, that is on domain width, length, and the amount of $+/-$ domains.

We discuss this behavior in terms of possible confinement patterns for vortices. The most likely picture is that the narrow and well-isolated magnetic domains confine vortices to single or double vortex chains, in which v-v distance is a power-law function of the domain width, and the minimal v-v distance is comparable to the magnetic penetration length. With increasing domain width and decreasing domain distance, the vortices most likely form the disordered Abrikosov vortex lattice.

*Current address: Materials Science Division, Argonne National Laboratory, Argonne, Illinois.

[1] U. Essmann and H. Träuble, Phys. Lett. A **24**, 526 (1967).

[2] M. Leghissa, L. A. Gurevich, M. Kraus, G. Saemann-Ischenko, and L. Ya. Vinnikov, Phys. Rev. B **48**, 1341 (1993).

[3] M. Menghini, Y. Fasano, F. de la Cruz, S. S. Banerjee, Y. Myasoedov, E. Zeldov, C. J. van der Beek, M. Konczykowski, and T. Tamegai, Phys. Rev. Lett. **90**, 147001 (2003).

[4] J. I. Martin, M. Vélez, A. Hoffmann, I. K. Schuller, and J. L. Vicent, Phys. Rev. Lett. **83**, 1022 (1999).

[5] J. E. Villegas, M. I. Montero, C.-P. Li, and I. K. Schuller, Phys. Rev. Lett. **97**, 027002 (2006).

[6] M. Velez, J. I. Martín, J. E. Villegas, A. Hoffmann, E. M. González, J. L. Vicent, and I. K. Schuller, J. Magn. Magn. Mater. **320**, 2547 (2008).

[7] A. K. Geim *et al.*, Nature (London) **390**, 259 (1997).

[8] I. V. Grigorieva, W. Escoffier, J. Richardson, L. Y. Vinnikov, S. Dubonos, and V. Oboznov, Phys. Rev. Lett. **96**, 077005 (2006).

[9] A. Bezryadin, Yu. N. Ovchinnikov, and B. Pannetier, Phys. Rev. B **53**, 8553 (1996).

[10] G. Karapetrov, J. Fedor, M. Iavarone, D. Rosenmann, and W. K. Kwok, Phys. Rev. Lett. **95**, 167002 (2005).

[11] M. V. I. F. Lyuksyutov and V. L. Pokrovsky, Adv. Phys. **54**, 67 (2005).

[12] A. Yu. Aladyshkin, A. V. Silhanek, W. Gillijns, and V. V. Moshchalkov, Supercond. Sci. Technol. **22**, 053001 (2009).

[13] L. N. Bulaevskii, E. M. Chudnovsky, and M. P. Maley, Appl. Phys. Lett. **76**, 2594 (2000).

[14] Yu. I. Bespyatykh, W. Wasilevski, M. Gajdek, I. P. Nikitin, and S. A. Nikitov, Sov. Phys.–Solid State **43**, 1827 (2001) [Fizika Tverdogo Tela **43**, 1754 (2001)].

[15] M. V. Milosevic, S. V. Yampolskii, and F. M. Peeters, Phys. Rev. B **66**, 174519 (2002).

[16] S. Erdin, I. F. Lyuksyutov, V. L. Pokrovsky, and V. M. Vinokur, Phys. Rev. Lett. **88**, 017001 (2001).

[17] E. B. Sonin, Phys. Rev. B **66**, 136501 (2002).

[18] R. Laiho, E. Lahderanta, E. B. Sonin, and K. B. Traito, Phys. Rev. B **67**, 144522 (2003).

[19] M. A. Kayali and V. L. Pokrovsky, Phys. Rev. B **69**, 132501 (2004).

[20] S. Erdin, Phys. Rev. B **73**, 224506 (2006).

[21] M. Lange, M. J. Van Bael, V. V. Moshchalkov, and Y. Bruynseraede, Appl. Phys. Lett. **81**, 322 (2002).

[22] M. Z. Cieplak, X. M. Cheng, C. L. Chien, and Hai Sang, J. Appl. Phys. **97**, 026105 (2005).

[23] M. Z. Cieplak Z. Adamus, A. Abal'oshev, I. Abal'osheva, M. Berkowski, X. M. Cheng, Hai Sang, and C. L. Chien, Phys. Status Solidi C **2**, 1650 (2005).

[24] V. Vlasko-Vlasov, U. Welp, G. Karapetrov, V. Novosad, D. Rosenmann, M. Iavarone, A. Belkin, and W.-K. Kwok, Phys. Rev. B **77**, 134518 (2008).

[25] A. Belkin, V. Novosad, M. Iavarone, J. Pearson, and G. Karapetrov, Phys. Rev. B **77**, 180506 (2008).

[26] V. K. Vlasko-Vlasov, U. Welp, A. Imre, D. Rosenmann, J. Pearson, and W. K. Kwok, Phys. Rev. B **78**, 214511 (2008).

[27] G. Karapetrov, M. V. Milošević, M. Iavarone, J. Fedor, A. Belkin, V. Novosad, and F. M. Peeters, Phys. Rev. B **80**, 180506(R) (2009).

[28] L. Y. Zhu, M. Z. Cieplak, and C. L. Chien, Phys. Rev. B **82**, 060503(R) (2010).

[29] V. Vlasko-Vlasov, U. Welp, W. Kwok, D. Rosenmann, H. Claus, A. A. Buzdin, and A. Melnikov, Phys. Rev. B **82**, 100502(R) (2010).

[30] M. Z. Cieplak, L. Y. Zhu, Z. Adamus, M. Kończykowski, and C. L. Chien, Phys. Rev. B **84**, 020514(R) (2011).

[31] M. Iavarone, A. Scarfato, F. Bobba, M. Longobardi, G. Karapetrov, V. Novosad, V. Yefremenko, F. Giubileo, and A. M. Cucolo, Phys. Rev. B **84**, 024506 (2011).

[32] C. Visani, P. J. Metaxas, A. Collaudin, B. Calvet, R. Bernard, J. Briatico, C. Deranlot, K. Bouzehouane, and J. E. Villegas, Phys. Rev. B **84**, 054539 (2011).

[33] E. Altshuler, Rev. Mod. Phys. **76**, 471 (2004).

[34] D. V. Denisov, D. V. Shantsev, Y. M. Galperin, E-M. Choi, H. S. Lee, S. I. Lee, A. V. Bobyl, P. E. Goa, A. A. F. Olsen, and T. H. Johansen, Phys. Rev. Lett. **97**, 077002 (2006).

[35] E. H. Brandt, Rep. Prog. Phys. **58**, 1465 (1995).

[36] M. Marchevsky, L. A. Gurevich, P. H. Kes, and J. Aarts, Phys. Rev. Lett. **75**, 2400 (1995).

[37] M. V. Indenbom, C. J. van der Beek, V. Berseth, W. Benoit, G. D'Anna, A. Erb, E. Walker, and R. Flükiger, Nature (London) **385**, 702 (1997).

[38] L. S. Uspenskaya and A. L. Rakhmanov, Phys. Rev. Lett. **100**, 137002 (2008).

[39] J. Guimpel, L. Civale, F. de la Cruz, J. M. Murduck, and I. K. Schuller, Phys. Rev. B **38**, 2342 (1988).

[40] C. A. Bolle, P. L. Gammel, D. G. Grier, C. A. Murray, D. J. Bishop, D. B. Mitzi, and A. Kapitulnik, Phys. Rev. Lett. **66**, 112 (1991).

[41] P. L. Gammel, D. J. Bishop, J. P. Rice, and D. M. Ginsberg, Phys. Rev. Lett. **68**, 3343 (1992).

[42] S. H. Brongersma, E. Verweij, N. J. Koeman, D. G. de Groot, R. Griessen, and B. I. Ivlev, Phys. Rev. Lett. **71**, 2319 (1993).

[43] V. O. Dolocan, P. Lejay, D. Mailly, and K. Hasselbach, Phys. Rev. B **74**, 144505 (2006).

[44] F. Laviano, L. Gozzelino, E. Mezzetti, P. Przyslupski, A. Tsarev, and A. Wisniewski, Appl. Phys. Lett. **86**, 152501 (2005).

[45] A. V. Silhanek, J. Gutierrez, R. B. G. Kramer, G. W. Ataklti, J. Van de Vondel, V. V. Moshchalkov, and A. Sanchez, Phys. Rev. B **83**, 024509 (2011).

[46] L. D. Cooley and A. M. Grishin, Phys. Rev. Lett. **74**, 2788 (1995).

[47] C. Reichhardt, J. Groth, C. J. Olson, S. B. Field, and F. Nori, Phys. Rev. B **54**, 16108 (1996).

[48] M. Tinkham, *Introduction to Superconductivity* (Dover, New York, 2004).

[49] B. W. Maxfield and W. L. McLean, Phys. Rev. **139**, A1515 (1965).

[50] J. Halbritter, Appl. Phys. A **43**, 1 (1987).

[51] C. P. Bean, Phys. Rev. Lett. **8**, 250 (1962); Rev. Mod. Phys. **36**, 31 (1964).

[52] W. T. Norris, J. Phys. D: Appl. Phys. **3**, 489 (1970); Y. Yang, T. Hughes, C. Beduz, D. M. Spiller, R. G. Scurlock, and W. T. Norris, Phys. C (Amsterdam) **256**, 378 (1996).

[53] E. H. Brandt, M. Indenbom, and A. Forkl, Europhys. Lett. **22**, 735 (1993); E. H. Brandt and M. Indenbom, Phys. Rev. B **48**, 12893 (1993); E. H. Brandt, *ibid.* **49**, 9024 (1994); Phys. Rev. Lett. **71**, 2821 (1993).

[54] E. Zeldov, J. R. Clem, M. McElfresh, and M. Darwin, Phys. Rev. B **49**, 9802 (1994).

[55] G. M. Maksimova, R. M. Ainbinder, and D. Y. Vodolazov, Phys. Rev. B **78**, 224505 (2008).

[56] E. H. Brandt, Phys. Rev. B **54**, 4246 (1996).

[57] M. Konczykowski, L. I. Burlachkov, Y. Yeshurun, and F. Holtzberg, Phys. Rev. B **43**, 13707 (1991); N. Chikumoto, M. Konczykowski, N. Motohira, and A. P. Malozemoff, Phys. Rev. Lett. **69**, 1260 (1992); E. Zeldov, A. I. Larkin, V. B. Geshkenbein, M. Konczykowski, D. Majer, B. Khaykovich, V. M. Vinokur, and H. Shtrikman, *ibid.* **73**, 1428 (1994).

[58] M. J. Van Bael, M. Lange, S. Raedts, V. V. Moshchalkov, A. N. Grigorenko, and S. J. Bending, Phys. Rev. B **68**, 014509 (2003).

[59] K. Harada, O. Kamimura, H. Kasai, T. Matsuda, A. Tonomura, and V. V. Moshchalkov, Science **274**, 1167 (1996).

[60] M. L. Latimer, G. R. Berdiyorov, Z. L. Xiao, W. K. Kwok, and F. M. Peeters, Phys. Rev. B **85**, 012505 (2012).

[61] M. V. Milosevic and F. M. Peeters, Phys. Rev. B **69**, 104522 (2004).